Journal of Materials Chemistry C

PAPER

View Article Online
View Journal | View Issue

Cite this: J. Mater. Chem. C, 2016, 4, 8930

Photoluminescence, cathodoluminescence and micro-Raman investigations of monoclinic nanometre-sized Y_2O_3 and Y_2O_3:Eu^{3+}

Daniel den Engelsen,[a] Terry G. Ireland,*[a] Paul G. Harris,[a] George R. Fern,[a] Paul Reip[b] and Jack Silver[a]

Received 21st June 2016,
Accepted 4th September 2016

DOI: 10.1039/c6tc02567f

www.rsc.org/MaterialsC

Herein we describe a large scale synthesis of nanosized, monoclinic Y_2O_3 and Y_2O_3:Eu^{3+} with 2 mol% Eu^{3+} in a plasma-discharge chamber. This high yield synthesis provided nanosized particles with dimensions between 5 nm to 50 nm, which were stable during shelf life at ambient conditions for more than 6 years. We assume that the Gibbs–Thomson effect is responsible for this unexpected high stability. Annealing at 950 °C completely transformed the monoclinic particles into the cubic phase, which was indicated by the photo- and cathodoluminescence emission spectra in addition to the much stronger light output. The undoped Y_2O_3 material was contaminated with Dy^{3+}, which showed characteristic and rather strong luminescence upon activation with a He–Ne laser at 632.8 nm, both at the Stokes and anti-Stokes side. Photoluminescence, cathodoluminescence and Raman spectra of the undoped and doped monoclinic nanocrystals were recorded and partially interpreted.

1. Introduction

Yttrium oxide (Y_2O_3) doped with trivalent Eu^{3+} is a well-known red emitting phosphor, which has found applications in fluorescent lamps and plasma display panels.[1,2] For application in high resolution displays it was thought that small phosphors particles would be necessary and this assumption increased interest to produce nanometre sized Y_2O_3:Eu^{3+}.[3] In the industrial applications of Y_2O_3:Eu^{3+} the Y_2O_3 host has the cubic (C type) phase, which is stable at ambient conditions and, most important, it has a rather high luminous efficiency when doped with Eu^{3+}. There are three other Y_2O_3 polymorphs, two of these have the A- and B-type rare earth sesquioxide structures that correspond to hexagonal and monoclinic phases respectively. The latter monoclinic B-type phase is formed at high pressure, whilst the hexagonal A-type structure has been reported to be formed at 2325 °C,[4] which is close to the melting temperature of Y_2O_3 at 2410 °C. Finally, the cubic Y_2O_3 polymorph transforms to a fluorite phase with disordered oxygen vacancies at 2308 °C.[5] In this study we focus on the monoclinic and cubic phases of Y_2O_3:Eu^{3+}, the high temperature phases will not be considered.

Literature on the synthesis and spectral characterisation of monoclinic Y_2O_3:Eu^{3+} is rather modest as compared to the vast literature on the cubic structure. The synthesis of monoclinic Y_2O_3 at ambient pressure conditions is not obvious; mostly the cubic phase will be obtained upon annealing powders at high temperature. Flame spray pyrolysis has been used to prepare nanometre-sized monoclinic Y_2O_3:Eu^{3+} or a mixture of the cubic and monoclinic phases.[4,6–10] By adjusting the residence time of the particles in the flame, Camenzind *et al.*[6] were able to determine the structure of the particles. Short residence times yielded small particle size with predominantly monoclinic structure. Qin *et al.* synthesised only monoclinic material when varying the residence time of the precursor in the flame.[7] Monoclinic Y_2O_3:Eu^{3+} nanometre-sized particles with approximately 10 nm in diameter were reported *via* different gas condensation methods.[11,12] Wang *et al.*[13] studied phase transitions in Y_2O_3 and Y_2O_3:Eu^{3+} as a function of pressure. Compression of cubic Y_2O_3:Eu^{3+} at room temperature and medium pressure yielded the monoclinic phase, which finally transformed into the hexagonal phase at very high pressure. Decompression produced the monoclinic phase only. Similar results for Y_2O_3:Eu^{3+} were found by Zhang *et al.*[14] by recording the photoluminescence as a function of pressure. From these works it can be concluded that once the monoclinic phase has been formed, it does not automatically return to the cubic phase. A plasma coating process for the fabrication of monoclinic undoped Y_2O_3 thin films was described by Gourlaouen *et al.*[15] These authors indicated that starting from cubic Y_2O_3 powder the yield of monoclinic Y_2O_3 was

[a] Centre for Phosphor and Display Materials, Wolfson Centre for Materials Processing, Brunel University London, Uxbridge, Middlesex, UB8 3PH, UK. E-mail: Terry.ireland@brunel.ac.uk
[b] Intrinsiq Materials Ltd, Building Y25, Cody Technology Park, Ively Road, Farnborough, Hampshire, GU14 0LX, UK

about 5% at a maximum. They also described the phase transition of monoclinic Y_2O_3 to cubic Y_2O_3 by annealing at high temperatures. The stability of the monoclinic phase of Y_2O_3 at room temperature and ambient pressure has been explained in terms of the Gibbs–Thomson effect,[4,11,16] which indicates that a very high specific surface area of the nano-particles increases the internal pressure to the same order of magnitude as that of the pressure required for the cubic-monoclinic transformation.

There are a number of problems encountered with the flame spray pyrolysis and gas condensation methods to produce Y_2O_3:Eu^{3+} nano-particles. First, the yields are usually low. Second, the resulting material in some cases is Y_2O_3:Eu^{3+} precursor that requires heat treatment to convert to the luminescent oxide: as a consequence this will cause particle growth and sintering between particles. Finally, in most cases mixtures of the monoclinic and cubic phases are obtained. Monoclinic bulk Y_2O_3 is not stable at ambient pressure, whereas nanometre-sized particles seem to be stable. This raises the questions (1) what would be the critical size to obtain stability and (2) what happens in a powder of monoclinic Y_2O_3 (doped or non-doped) with a grain size distribution from micrometres to nanometres? These two latter questions were also important in starting this study. Here we describe the synthesis of discrete nanometre sized-particles of Y_2O_3 and Y_2O_3:Eu^{3+} using a high-temperature plasma method that provides a high product yield. The original idea in choosing this method was to make nanometre-sized cubic Y_2O_3 doped with rare earth elements on a large scale. As it turned out in the course of this work, this synthesis provided primarily the monoclinic phase of Y_2O_3, which was quite unexpected. The materials were characterised using X-ray powder diffraction (XRD) and transmission electron microscopy (TEM), both in stationary and scanning modes. In the case of Y_2O_3:Eu^{3+}, cathodoluminescence imaging was carried out and the photoluminescence (PL), cathodoluminescence (CL) and Raman scattering properties were also studied.

2. Materials and methods

2.1. Materials

Starting materials, Y_2O_3 powder and europium oxide (Absco Ltd, Haverhill, UK, 99.99%) were used without additional purification. The monoclinic Y_2O_3 and Y_2O_3:Eu^{3+} materials were produced according to Intrinsiq's patented plasma process[17] by wet mixing europium oxide and cubic yttrium oxide in a tubular mixer, followed by drying and then a secondary crushing process to break the materials down to sub 10 μm. This feedstock of precursors was fed by gravity into the hot plasma (>9000 °C), in which it vaporised and condensed to form the nanometre-sized phosphor particles.

Typical parameters for producing about 1 kg of material were 80 kW torch power, with 2000 l min^{-1} argon flow rate to cool the materials down to suitable temperature for quality testing and collection on a set of nano-porous stainless steel filters, before blowing back to release and collect. Cubic nanometre-sized Y_2O_3:Eu^{3+}, which was measured for reference purposes only, was synthesized according to the urea precipitation method, which has been described in detail in our previous work.[18–20]

2.2. Methods and equipment

XRD measurements were made using a Bruker D8 powder diffractometer fitted with a Lynxeye multi-element detector and operating in the theta–theta scan mode. The powders were placed in an A100B3B Air tight XRD holder and the data were recorded from $5^\circ < 2\theta < 100^\circ$ at 293 K. Copper radiation was used and the emission profile calibrated using NIST 660a LaB_6 line profile standard and line position was calibrated using a corundum standard from Bruker. The line profile was analysed with Bruker Diffrac Plus Evaluation version 13,0,0,2 and the data were refined using Bruker's AXS Topas version 3.0 Rietveld refinement computer software. The background was fitted with a Chebychev polynomial.

For the studies in the TEM copper grids coated with thin carbon films having small holes (holey carbon films) were used as substrates: these are transparent to the high-energy electrons. TEM was carried out using a JEOL 2100F (Japan). The TEM was equipped with a Vulcan™ CL detector of Gatan (USA) for imaging and spectroscopic purposes. This system used a Czerny-Turner spectrometer with back-illuminated CCD and a grating with 1200 lines per mm (blazed at 500 nm) for collection of CL emission spectra. Light was collected from the sample using a mirror above and below the sample, which enabled a solid angle of about 5 sr, which is almost half of a sphere.

For recording CL spectra samples were mounted in two different high vacuum chambers at a vacuum level of $\approx 3 \times 10^{-6}$ mbar using Kimball Physics Inc. (USA) electron guns and associated power supplies over the ranges of electron beam voltages of 1–5 kV and 3–15 kV respectively. The electron guns had the ability to focus and defocus the beam over a range of current densities. The luminous efficiency and energy efficiency were measured with a uniform electron beam (by defocusing) at current densities between 1 and 10 μA cm^{-2}. Deflection plates enabled optimum positioning of the electron beam on the sample and a ZnO:Zn reference. The latter being a non-charging thin film of ZnO:Zn powder on ITO to adjust the current in the thin powder layers of Y_2O_3 and Y_2O_3:Eu^{3+}: in this way we could cope with the effect of charging of the non-conductive Y_2O_3 layers as explained in our previous work.[20]

Radiance and luminance of CL were measured with a Jeti Radiometer (Spectrobos 1200, Germany) between 380 and 780 nm as described earlier.[18,20] PL- and CL-spectra were measured with a Bentham Instruments dual monochromator system equipped with 0.37 mm slits. Emission spectra were recorded in the range of 300 nm to 800 nm in steps of 0.2 nm. The wavelength error of the Bentham spectrometer was estimated to be ±0.5 nm. Raman and laser induced fluorescence spectra of the samples were measured with a Horiba Jobin Yvon Labram HR monochromator by excitation with a He–Ne laser at 298 K. The wavelength error of the Labram monochromator was smaller: about ±0.2 nm.

3. Results

The nanometre-sized particles of Y_2O_3 and Y_2O_3:Eu^{3+} obtained by high-temperature plasma synthesis were white under the D50 lamp, similar to that of the bulk material; using 254 nm light excitation only the europium-doped material displayed red luminescence. Energy dispersive X-ray analysis (EDX) of the undoped and doped samples showed some contamination (<0.5%) of Fe and Cu, the Fe was probably from the stainless steel rings in the reaction chamber and the origin of the Cu was from the nozzles of the plasma discharge flame. The Eu^{3+} concentration of the doped sample was about 2%. No other contaminations could be detected with this technique.

Fig. 1 shows the XRD diagrams of the high-temperature plasma synthesised Y_2O_3 and Y_2O_3:Eu^{3+} nano-particles. They were both predominantly composed of the monoclinic (B-type) phase (89% and 93%) with some cubic (C-type) phase (11% and 7%) when compared to a reference pattern. This composition of the samples was calculated from the XRD graphs using Bruker's AXS Topas version 3.0 Rietveld refinement computer software. The yield of monoclinic phase was much higher than that obtained by Gourlaouen *et al.*[15] with a plasma spray gun.

The undoped and doped compounds had similar crystallite sizes of 17.7 nm and 17.9 nm for the monoclinic phase and 30.0 nm and 45.0 nm for the cubic phase, determined by XRD line-broadening analysis using Scherrer's method, which is included in the Topas software.

The TEM image in Fig. 2a represents the as-synthesised monoclinic Y_2O_3 nano-particles, which have sizes from 5 nm to 50 nm. This agrees with the crystallite size as determined from the XRD diagrams. Fig. 2a shows that these particles were sintered and formed a large cluster. Since the image of the Y_2O_3:Eu^{3+} particles is essentially identical to that of the undoped particles, it will not be reproduced here. The Scanning TEM (STEM) images shown in Fig. 2b and c are at a smaller magnification. Recording of the panchromatic image (Fig. 2c) was possible by maximizing the current in the e-beam.

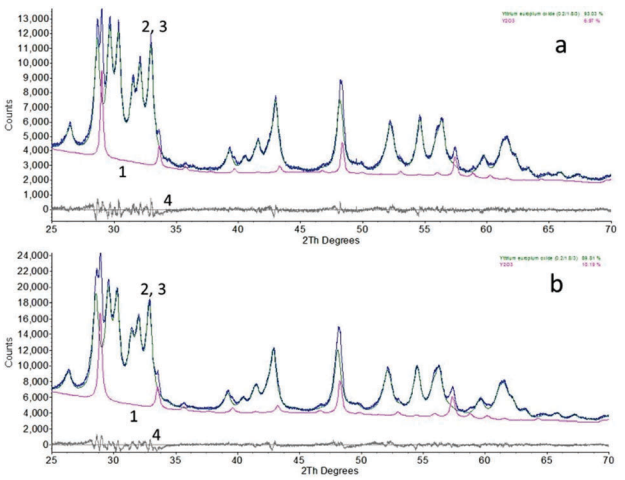

Fig. 1 XRD patterns of Y_2O_3:Eu^{3+} (a) and undoped Y_2O_3 (b) high-temperature plasma synthesised nano-particles. Spectra 1: cubic phase, spectra 2, 3: raw data and fitted XRD-diagrams; 4: difference between spectra 2 and 3.

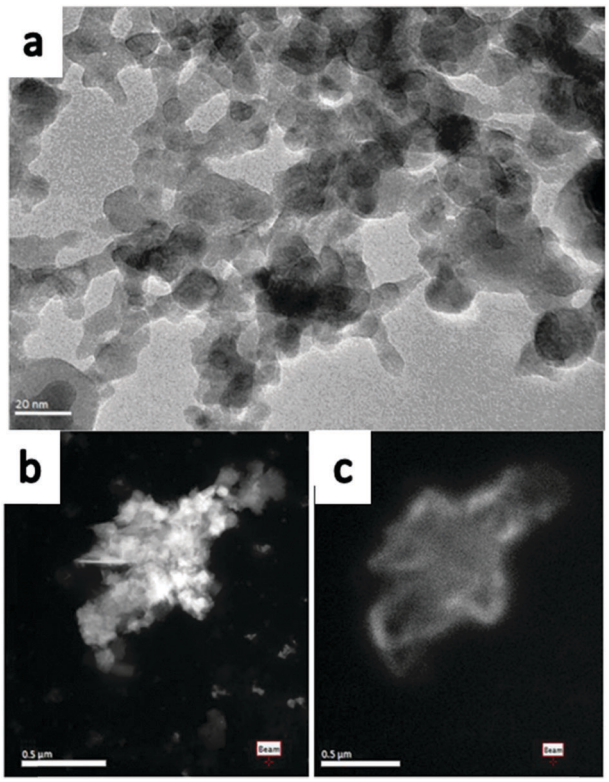

Fig. 2 TEM image of monoclinic (a) Y_2O_3 nano-particles, (b) STEM image of monoclinic Y_2O_3:Eu^{3+} recorded at 200 keV −170 °C, (c) panchromatic CL image of particles shown in (b) recorded at same conditions.

Some larger particles of about 250 nm were observed to be present in the products due to precursor oxides passing directly through the plasma without totally evaporating to ions, presumably due to being too large initially as shown in Fig. 3a. This figure is a STEM image at 200 kV and temperature of −170 °C of doped monoclinic material. Since the large particles differ substantially from the smaller monoclinic-phase particles shown in Fig. 2a, we conclude that these particles are non-reacted cubic Y_2O_3 precursor material. A proof of this hypothesis is shown in Fig. 3b, which is the CL spectrum of the large particle, indicated with the red arrow in Fig. 3a, recorded with the Gatan spectrometer connected to the TEM. This spectrum shows only the intrinsic blue emission of cubic Y_2O_3 between 400 and 500 nm upon excitation with high energetic electrons.[21] From this spectrum it can be concluded that the large spherical particle did not contain the Eu-dopant; routinely a strong Eu^{3+} emission would be observed from this sized particle. Another indication that this particle must be cubic Y_2O_3 is the fact that 2% Eu^{3+} will almost quench the intrinsic Y_2O_3 emission.[21] The mere presence of this intrinsic emission is thus a proof that the particle is undoped Y_2O_3 precursor. The evidence presented in Fig. 3a and b indicates that the composition of the synthesized samples calculated above from the XRD-data is somewhat misleading, because the samples contained a small quantity of non-reacted cubic Y_2O_3 particles. Since these precursor particles did not

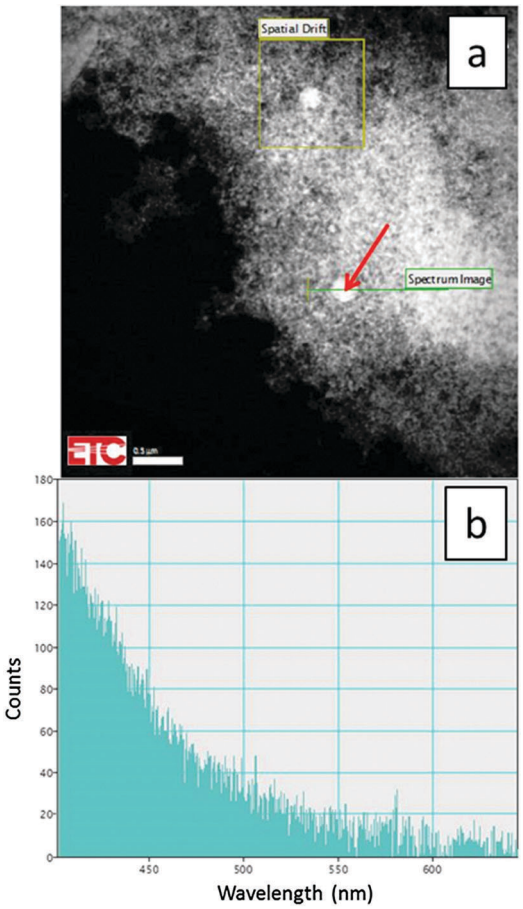

Fig. 3 STEM image (a) of monoclinic Y_2O_3:Eu^{3+} sample at 200 keV and −170 °C with large non-reacted cubic Y_2O_3 particles (one indicated by red arrow). CL spectrum (b) of large cubic particle recorded at same conditions with Gatan spectrometer between 400 and 650 nm.

contain Eu^{3+}, the percentage of monoclinic Y_2O_3:Eu^{3+} is substantially larger than 93% as compared to cubic Y_2O_3:Eu^{3+}. In the discussion of Fig. 12a hereafter, we shall indicate that the percentage of monoclinic Y_2O_3:Eu^{3+} is more than 99% as compared to cubic Y_2O_3:Eu^{3+} when the quantity of non-reacted precursor material is ignored.

In Fig. 4 XRD diagrams of annealed monoclinic Y_2O_3:Eu^{3+} nanoparticles over the temperature range 800 °C to 1000 °C for 60 minutes are presented. From these diffractograms the transformation from monoclinic to cubic phase is shown to be partial at 900 °C and complete at 1000 °C. This agrees with the differential scanning calorimetry data published by Zhang *et al.*[4] that indicates a phase transition from monoclinic to cubic Y_2O_3 between 850 °C and 950 °C. As a consequence of the annealing treatments, an increase in crystallite size was observed: at 800 °C the crystallite size was 25.6 nm and 34.3 nm, increasing to 48.5 nm and 42.7 nm at 900 °C for the monoclinic and cubic phases respectively and 63.3 nm at 1000 °C for the cubic phase.

The TEM images shown in Fig. 5a–c refer to monoclinic Y_2O_3:Eu^{3+} samples annealed at 800 °C, 900 °C and 1000 °C for 60 minutes. It can be seen that particle growth occurs with an

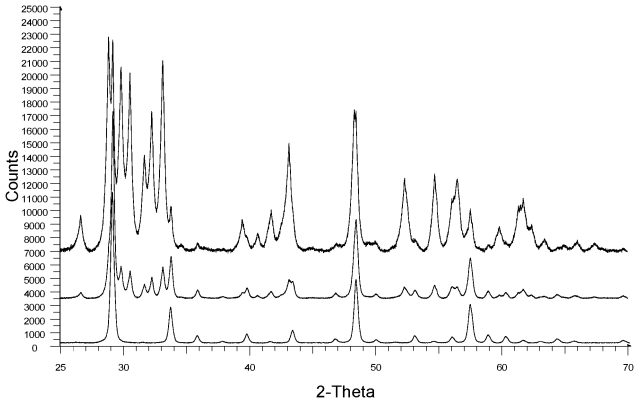

Fig. 4 XRD patterns of monoclinic Y_2O_3:Eu^{3+} plasma discharge nanoparticles after annealing at 800 °C (top), 900 °C (middle) and 1000 °C (bottom) for 60 minutes.

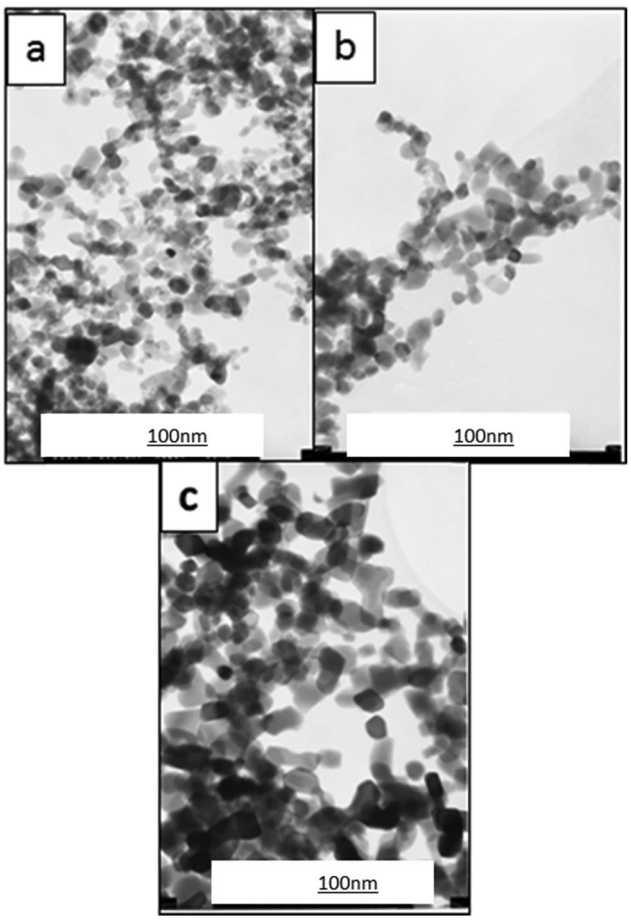

Fig. 5 TEM images of Y_2O_3:Eu^{3+} samples annealed at (a) 800 °C (b) 900 °C and (c) 1000 °C for 60 minutes.

increase in annealing temperature. After annealing above the monoclinic to cubic phase transition temperature, which occurs between 850 °C to 950 °C, the particles are observed to grow considerably in size to between 25 nm to 100 nm.

The normalised PL excitation and emission spectra of the high-temperature plasma synthesised Y_2O_3:Eu^{3+} nano-particles

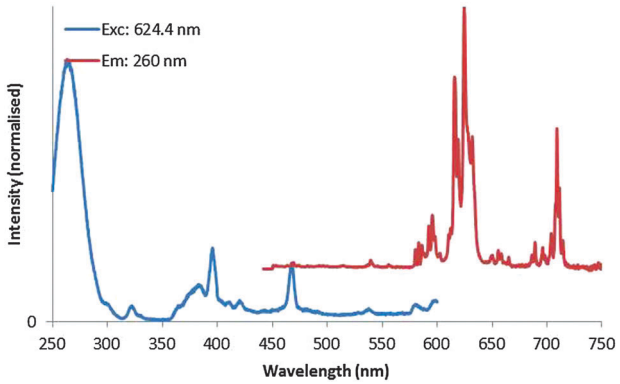

Fig. 6 Normalised PL excitation (monitored at 624 nm, normalised at 260 nm) and emission (excited at 260 nm, normalised at 624 nm) spectra of monoclinic Y_2O_3:Eu^{3+} nano-particles.

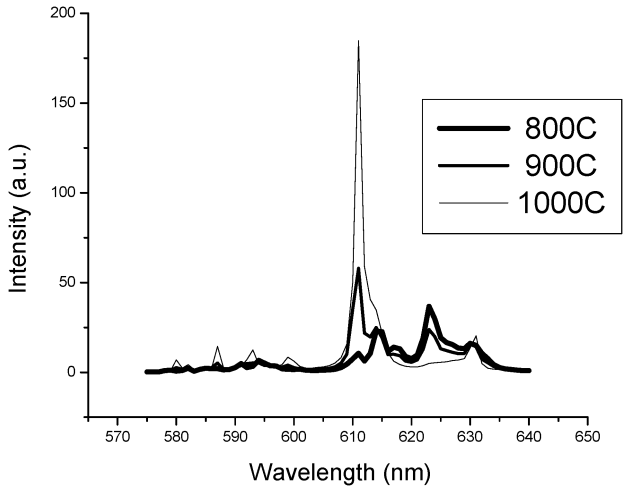

Fig. 7 PL emission spectra (excitation wavelength 254 nm) of the plasma discharge process monoclinic Y_2O_3:Eu^{3+} nano-particles after annealing at 800 °C, 900 °C and 1000 °C for 60 minutes illustrating the phase transition from monoclinic to cubic.

are presented in Fig. 6. The sample was excited using 260 nm UV-light; the excitation spectrum was collected monitoring the 624 nm peak. The emission spectrum is representative of the Eu^{3+} ion in a monoclinic Y_2O_3 host lattice.

A comparison of various PL emission spectra is presented in Fig. 7 for the high-temperature plasma synthesised monoclinic Y_2O_3:Eu^{3+} nano-particles after annealing for a period of 60 minutes at temperatures of 800 °C, 900 °C and 1000 °C. These spectra illustrate the transition from monoclinic to cubic phase that occurs between 850 °C and 950 °C: these spectra agree favourably with the results represented in Fig. 4. The intensity of light emitted under PL excitation from monoclinic Y_2O_3:Eu^{3+} phosphor is much weaker than that from a cubic Y_2O_3:Eu^{3+} phosphor; this is demonstrated by the relative intensities of the spectra shown in Fig. 7 for identical phosphor screen weights and in Fig. 10, to be discussed hereafter.

Fig. 8 shows the PL and CL spectra of monoclinic Y_2O_3:Eu^{3+}. The PL spectrum was obtained by exciting with 260 nm

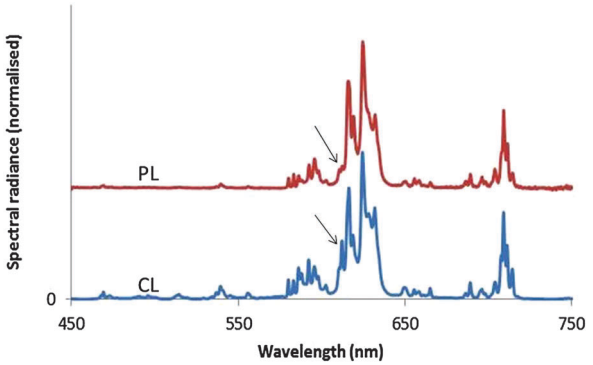

Fig. 8 Cl spectrum (bottom) and PL spectrum (top) of nanosized monoclinic Y_2O_3:Eu^{3+}. The CL spectrum was recorded at 15 keV beam energy and current density of 1 μA cm^{-2}. Both spectra have been normalised to unity at 624 nm, the strongest peak of the $^5D_0 \rightarrow {}^7F_2$ transition manifold of monoclinic Y_2O_3:Eu^{3+}. The arrows indicate the $^5D_0 \rightarrow {}^7F_2$ transition of cubic Y_2O_3:Eu^{3+} at 611 nm, which is the only transition of the cubic phase that can be distinguished in these spectra.

ultraviolet light. The CL spectrum refers to a sample that was bombarded with 15 keV electrons; the current density was 1 μA cm^{-2}. The further the emission lines in the CL spectrum are from the strong peak at 624 nm, the stronger they are as compared to the corresponding lines in the PL spectrum. The strong $^5D_0 \rightarrow {}^7F_2$ line of the cubic phase is the only transition of this material that can be observed in the spectra of Fig. 8. It has been indicated with an arrow. This transition is more clearly visible in Fig. 12a. In Fig. 9 we have depicted the CL spectra of nanosized cubic and monoclinic Y_2O_3:Eu^{3+}. Both spectra were recorded at identical conditions: beam energy of 15 keV and current density of 1 μA cm^{-2}.

The assignments of the transition manifolds that are clearly noticeable have been indicated in Fig. 9. The wavelength difference of corresponding transition clusters between monoclinic and cubic Y_2O_3:Eu^{3+} is small, which is to be expected for intra-4f transitions of the Eu^{3+} ion. The table in Fig. 9 lists the lowest energy levels (in cm^{-1}) for the indicated electronic states of Eu^{3+} in the two hosts. The levels for monoclinic Y_2O_3:Eu^{3+}

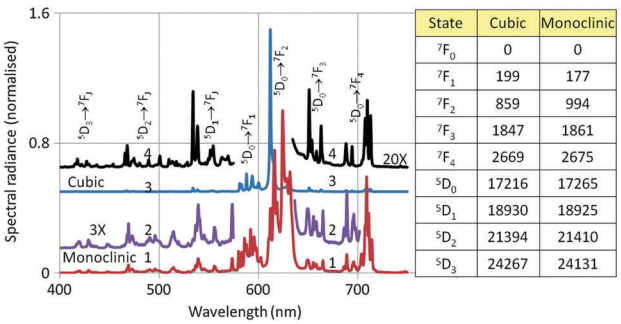

State	Cubic	Monoclinic
$^7F_0$	0	0
$^7F_1$	199	177
$^7F_2$	859	994
$^7F_3$	1847	1861
$^7F_4$	2669	2675
$^5D_0$	17216	17265
$^5D_1$	18930	18925
$^5D_2$	21394	21410
$^5D_3$	24267	24131

Fig. 9 Comparison of CL spectra of cubic and monoclinic Y_2O_3:Eu^{3+}. Spectra (1) and (2) refer to monoclinic Y_2O_3:Eu^{3+}, while spectra (3) and (4) refer to cubic Y_2O_3:Eu^{3+}. Spectrum (2) is three times vertically magnified from (1) while (4) is twenty times magnified from (3). In the table the lowest energy levels (in cm^{-1}) of some ^7F_J and ^5D_J electronic states of Eu^{3+} in cubic and monoclinic Y_2O_3 are compared.

have been calculated from the spectra represented in Fig. 9, while the levels for the cubic phase are from Wen *et al.*[22] and Gruber *et al.*[23] The largest difference between the cubic and monoclinic material was found for the level of $^7F_2$: for the other states the levels are quite similar. In spite of the similarity in energy, the spectra of the cubic and monoclinic phase look quite different, especially for the $^5D_0 \rightarrow {}^7F_2$ transition manifold. In cubic Y_2O_3:Eu^{3+} the peak with the strongest spectral radiance has the lowest wavelength (611 nm), while in monoclinic Y_2O_3:Eu^{3+} the peak with the strongest spectral radiance is at 624 nm, which is the 5th peak of the $^5D_0 \rightarrow {}^7F_2$ manifold: this can be observed more clearly in Fig. 12a, to be discussed later. The differences in spectral radiance between the peaks of a particular transition manifold exemplify the sensitivity of Eu^{3+} to the coordination: in the cubic material Eu^{3+} is 6-fold coordinated, whereas in monoclinic Y_2O_3 it is 7-fold coordinated.[12]

The spectra of monoclinic Y_2O_3:Eu^{3+} synthesised by plasma discharge in Fig. 8 and 9 show the $^5D_0 \rightarrow {}^7F_2$ transition of the cubic material at 611 nm, which is substantially larger in the CL spectrum than in the PL spectrum. This is a spectroscopic confirmation of the XRD-results that the high-temperature plasma Y_2O_3:Eu^{3+} was not purely monoclinic. The first PL spectrum of the monoclinic sample was recorded in 2009 and the most recent in May 2015. Since there was no change in the height of this 611 nm peak with respect to the heights of neighbouring peaks, it can be concluded that the nanosized monoclinic Y_2O_3:Eu^{3+} crystals with the rather small particles are stable during shelf life at ambient conditions for a long time.

Luminance and radiance of the samples were measured with the Jeti Radiometer upon electron bombardment between 5 and 15 kV and current density between 1 and 3 μA cm^{-2}. From the luminance the luminous efficacy can be calculated, while the energy efficiency is calculated from the measured radiance.[18] Luminous efficacy results are presented in Fig. 10 for CL measurements at electron beam energies between 1 and 15 keV. The curve of the luminous efficacy *versus* beam voltage does not vary strongly between 5 and 15 kV, indicating that at low beam voltages monoclinic Y_2O_3:Eu^{3+} is already luminescing quite well. However, its luminous efficacy is about 25 times weaker at 15 kV than that of nanosized cubic Y_2O_3:Eu^{3+}[18] which makes this phosphor not particularly attractive for industrial applications. The energy efficiency of the CL between 380 and 780 nm of monoclinic Y_2O_3:Eu^{3+} at 15 kV is found to be 0.2%, which 20 times smaller than that of cubic Y_2O_3:Eu^{3+}.[18] Curve 2 in Fig. 10 underpins the information presented in Fig. 7 that the total light output increases as the structure transforms from the monoclinic through a mixed monoclinic/cubic phase with increasing temperature treatment and finally to a pure cubic phase.

In Fig. 11 the CL and laser-activated spectra of undoped and doped monoclinic Y_2O_3 nanometre-sized particles are presented. The laser-activated spectrum of the undoped material in Fig. 11a shows surprisingly a strong luminescence signal at the anti-Stokes side (543 nm) of the He–Ne laser and at the Stokes side (756 nm) we detected also a rather strong luminescence. These two luminescence clusters are assigned to Dy^{3+}, which was a contaminant of the Y_2O_3 starting material for the high-temperature plasma synthesis, present in the ppm-range. As mentioned above, this contamination could not be detected with our EDX equipment. The CL spectrum in Fig. 11a shows Dy^{3+} transitions at 573 nm and 485 nm. The Dy^{3+} transitions will be discussed hereafter; first we shall concentrate on the laser-activated spectrum of Eu^{3+}. Since the laser-activated spectra have been recorded with a high resolution Horiba Jobin Yvon Labram spectrometer, we shall represent some details of the spectra shown in Fig. 11b at larger abscissas in Fig. 12.

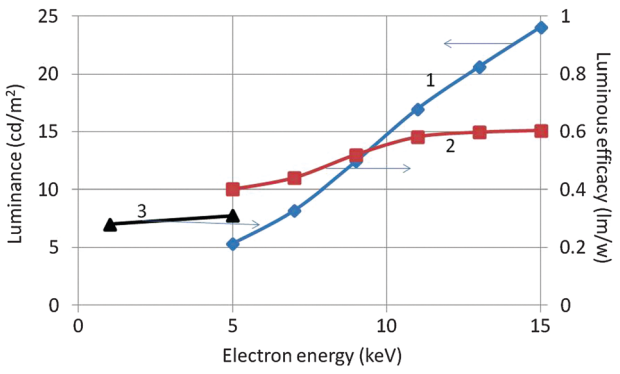

Fig. 10 Luminance (curve 1) and luminous efficacy (curve 2 and line 3) of nanosized monoclinic Y_2O_3:Eu^{3+} *versus* energy of the electron beam. Current density was 1 μA cm^{-2}. Substrate for the sample of (3) was: Al, substrate for the sample (2) was indium-tin (10%) oxide (ITO).

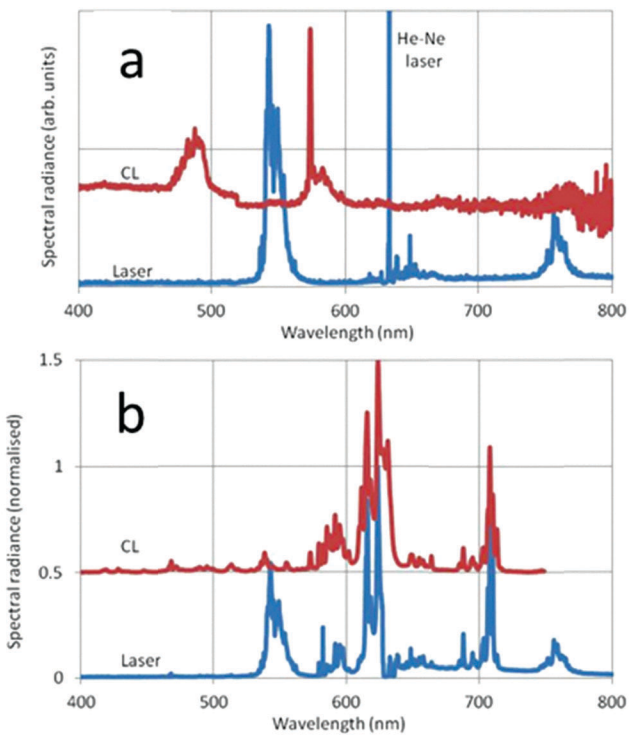

Fig. 11 CL and laser-activated spectra of undoped monoclinic Y_2O_3 (a) and Eu^{3+} doped monoclinic Y_2O_3 (b). The CL spectra were recorded at 15 keV beam energy and current density of 1 μA cm^{-2}. The He–Ne line in (b) has been deleted.

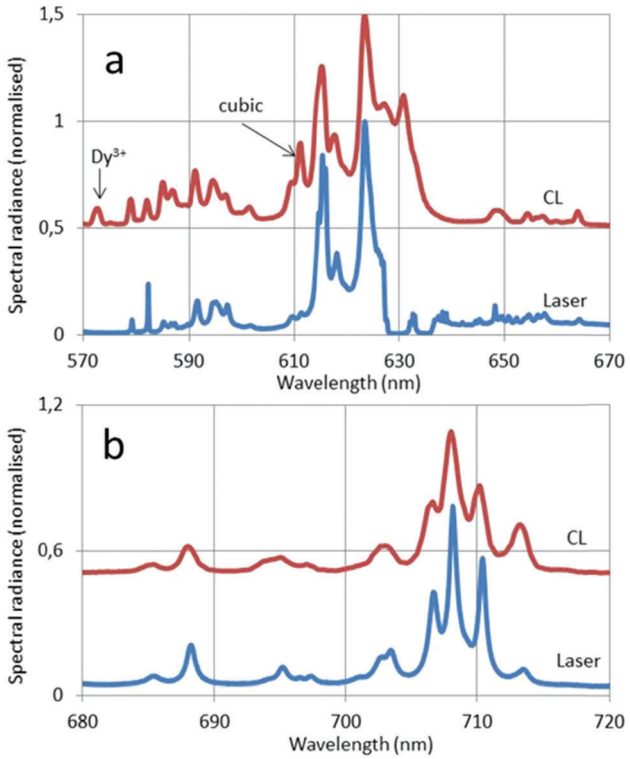

Fig. 12 CL and laser-activated spectra of Eu^{3+} doped monoclinic. (a) From 570–670 nm; (b) from 680–720 nm. The CL spectra were recorded at 15 keV beam energy and current density of 1 μA cm^{-2}. The He–Ne line in (a) has been deleted. Normalisation has been made towards the $^5D_0 \rightarrow {}^7F_2$ peak at 624 nm.

In Fig. 12a the $^5D_0$–$^7F_2$ transition of the cubic phase at 611 nm has been indicated with an arrow. The spectral radiance of this transition is about four times smaller than the spectral radiance of the $^5D_0$–$^7F_2$ transition of the monoclinic phase at 624 nm. From this result we can estimate the amount of cubic phase in the sample doped with Eu^{3+}.

Let R_{611}(cubic) be the radiance of the $^5D_0$–$^7F_2$ transition of the cubic phase and R_{624}(mono) the radiance of the corresponding transition for the monoclinic phase, x be the weight fraction of cubic phase, η_c and η_m be the energy efficiencies of the cubic and monoclinic materials respectively and f_c and f_m be the (fractional) contributions of the 611 nm and 624 nm transitions to the energy efficiency for the cubic and monoclinic materials respectively. From the low resolution spectra recorded with the Jeti radiometer we found that $f_c = 0.56$ and $f_m = 0.41$. This implies that the contribution of the $^5D_0$–$^7F_2$ transition of the cubic phase to the energy efficiency is 1.36 times larger than that for the monoclinic phase. The fraction x is calculated from the following equation

$$\frac{R_{611}(\text{cubic})}{R_{624}(\text{mono})} = \frac{x\eta_c f}{(1-x)\eta_m f_m} \approx 0.25$$

Since η_c is 20 times larger than η_m we get $x \approx 0.9\%$: in other words, the yield of monoclinic phase by the plasma discharge synthesis is >99% when we ignore the non-reacted Y_2O_3 precursor.

Both Fig. 8 and 12a show that only the CL spectrum of monoclinic Y_2O_3:Eu^{3+} exhibits clearly the $^5D_0$–$^7F_2$ transition of the cubic phase at 611 nm. This latter transition is much weaker in the PL and laser-activated spectra. The excitation mechanism for the latter two spectra is more subtle and depends strongly on the energy of the exciting radiation. Since we had no efficiency information for the PL and laser-activated spectra, we had to base our yield calculation on the CL-data only.

The $^5D_0 \rightarrow {}^7F_2$ peak at 615 nm in Fig. 8 and 9 is split in the laser-activated spectrum of Fig. 12a and consists of three peaks at 614.6 nm, 615.4 nm and 616 nm. The laser-activated spectrum of nanosized cubic Y_2O_3:Eu^{3+} was reported by Silver *et al.*[24] They showed that besides Stokes and anti-Stokes luminescence, excitation of high-energy levels is possible through the absorption of two laser photons. This mechanism can also explain the presence of some (very) weak transitions in the laser-activated spectrum of monoclinic Y_2O_3:Eu^{3+} at 467 nm, 490 nm and 513 nm, which belong to the $^5D_2 \rightarrow {}^7F_J$ manifold of Eu^{3+}. In Fig. 12a we have indicated the Dy^{3+} transition in the CL spectrum at 573 nm with an arrow.

We shall now discuss the Dy^{3+} peaks in the laser-activated and CL spectra of Fig. 11a and b. The anti-Stokes cluster at 543 nm (18 412 cm^{-1}) is attributed to the $^4I_{15/2} \rightarrow {}^6H_{13/2}$ electronic transition of Dy^{3+}, while the Stokes cluster at 756 nm (13 224 cm^{-1}) is due to $^4F_{9/2} \rightarrow {}^6H_{9/2}$. These transitions have been visualized in Fig. 13 by the green and red downward arrows respectively.

The assignments reported here are based on the electronic levels of Dy^{3+} in cubic Y_2O_3,[25] which deviate slightly from the values measured by us in monoclinic Y_2O_3. Only the lowest levels of the manifolds have been represented in Fig. 13. The excitation to the $^4I_{15/2}$ and $^4F_{9/2}$ levels of Dy^{3+} is supposed to be controlled by the excited states absorption (ESA) process, as explained by Silver *et al.*[24] First the $^6F_{1/2}$ level is populated by the He–Ne laser. The energy trickles radiationless down to the

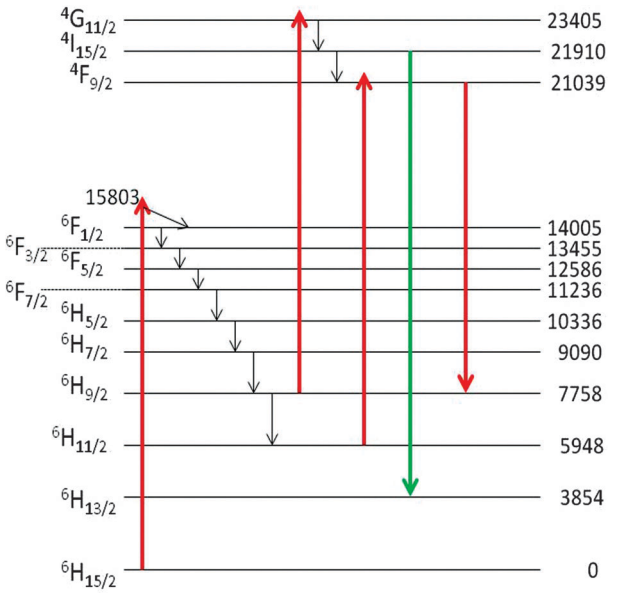

Fig. 13 Schematic energy level diagram of cubic Y_2O_3:Dy^{3+} and the proposed excitation and emission transitions. The energy levels, indicated in cm^{-1}, are from Chang *et al.*[25]

$^6H_{9/2}$ and $^6H_{11/2}$ levels, from where it can be excited to either the $^4F_{9/2}$ or the $^4G_{11/2}$ level by absorption of another He–Ne photon. We consider this ESA process more likely than an alternative route *via* the absorption of two He–Ne photons. The reason is that (1) a two-photon absorption would probably lead to very weak luminescence of Dy^{3+} and (2) the ESA process requires excitation of the $^6F_{1/2}$ state, which is almost resonant with the He–Ne laser: it should be kept in mind that only the lowest level of the electronic states are indicated in Fig. 13. We have checked this hypothesis by using a laser at 532 nm. When activating the undoped monoclinic Y_2O_3 with this laser we did not observe the characteristic transitions at 543 nm and 756 nm (not shown here). Hence, it can be concluded that the mechanism indicated in Fig. 13 for the luminescence of the monoclinic Y_2O_3:Dy^{3+} is likely.

The CL spectrum of Fig. 11a shows different Dy^{3+} transitions. The peak at 573 nm (17 428 cm^{-1}) is due to $^4F_{9/2} \rightarrow {}^6H_{13/2}$, while the cluster at 482 nm (20 756 cm^{-1}) is attributed to $^4F_{9/2} \rightarrow {}^6H_{15/2}$. These latter transitions were also recorded by Vetrone *et al.*[26] in cubic Y_2O_3:Dy^{3+} with PL. The differences between the Dy^{3+} levels of cubic and monoclinic Y_2O_3:Dy^{3+} are rather small: the energy values indicated in the diagram of Fig. 13 refer to the lowest values of the manifolds and represent the right-hand sides of the recorded transitions clusters. The Dy^{3+} peak at 573 nm has been erased in the CL spectrum represented in Fig. 8 in order to avoid confusion, whereas it still present in the CL spectrum of the monoclinic material in Fig. 9.

In Fig. 14 we have depicted the Raman spectrum of undoped monoclinic Y_2O_3. In this figure spectrum (1) is the conventional Raman spectrum at the Stokes-side of the He–Ne line. Spectrum (2) has been derived from (1) by multiplication with the Boltzmann factor: $e^{-h\nu/kT}$, in which h is Planck's constant, ν is the frequency of the actual Raman line, k is Boltzmann's constant and T is 298 K. Spectrum 3 in Fig. 14 is the anti-Stokes Raman spectrum. As expected, the spectra (2) and (3) are largely identical; nevertheless, spectrum (2) and the anti-Stokes spectrum (3) differ substantially at $\nu < 150$ cm^{-1}: the Raman peaks at 96 cm^{-1}, 106 cm^{-1} and 115 cm^{-1} are not observed in the anti-Stokes spectrum. The reason for this difference is unknown.

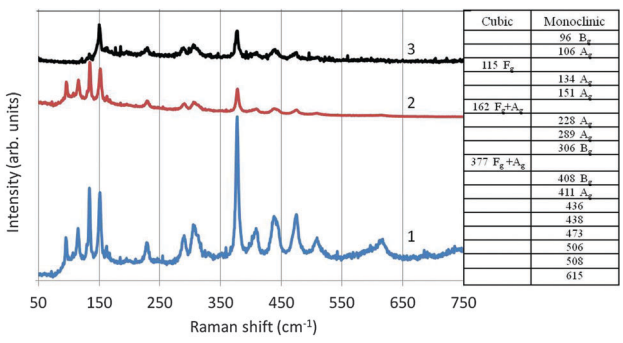

Cubic	Monoclinic
	96 B_g
	106 A_g
115 F_g	
	134 A_g
	151 A_g
162 F_g+A_g	
	228 A_g
	289 A_g
	306 B_g
377 F_g+A_g	
	408 B_g
	411 A_g
	436
	438
	473
	506
	508
	615

Fig. 14 Raman spectrum of undoped monoclinic Y_2O_3 (1). Spectrum (2) is derived from (1) by multiplying with the Boltzmann factor. Spectrum (3) is the anti-Stokes Raman spectrum. The table (values in cm^{-1}) represents an incomplete assignment of the recorded Raman spectrum (1) of Y_2O_3.

In Fig. 14 we have also represented a table with an assignment of the Raman lines at $\nu < 411$ cm^{-1}. As mentioned above, the high-temperature plasma synthesis of Y_2O_3 did not yield pure monoclinic material, but also some cubic crystals. Raman lines for cubic Y_2O_3:Eu^{3+} are at 115 cm^{-1}, 162 cm^{-1} and 377 cm^{-1}, as indicated by Withnall *et al.*[27] The other Raman lines of cubic Y_2O_3:Eu^{3+} detected by Withnall *et al.* were too weak to be observed in our sample with only about 15% cubic material. The assignment of the monoclinic Raman lines is based on the interpretation of the Raman spectra of monoclinic Sm_2O_3, Eu_2O_3 and Gd_2O_3 by Gouteron *et al.*[28]

4. Conclusions

The main conclusions of this investigation of monoclinic Y_2O_3 and Y_2O_3:Eu^{3+} by XRD, TEM and spectroscopy are: (1) the yield of monoclinic phase by plasma discharge synthesis is more than 99% if we ignore the non-reacted Y_2O_3 precursor and (2) nanometre-sized monoclinic material is stable during shelf life at ambient conditions. We attribute this stability to the small particle size (between 5 and 50 nm) of the monoclinic materials. We found that the luminous efficiency of monoclinic Y_2O_3:Eu^{3+} upon electron excitation is about 25 times less than that of the cubic material and we observed the transition from the monoclinic phase to the cubic phase at about 900 °C by XRD and PL. Since the starting Y_2O_3 material for the high-temperature plasma synthesis of monoclinic Y_2O_3 was contaminated with a small quantity of Dy^{3+}, we were able to measure and interpret the laser-activated spectrum of monoclinic Y_2O_3:Dy^{3+}. Hence, this study has also shown that excitation of inorganic crystals with a He–Ne laser provides an extremely sensitive and specific measuring method for the spectroscopic determination of traces of Dy^{3+}.

Acknowledgements

We are grateful to the EPSRC and the Technology Strategy Board (TSB) for funding the PURPOSE (TP11/MFE/6/I/AA129F; EPSRC TS/G000271/1), CONVERTED (JeS no. TS/1003053/1) and PRISM (EP/N508974/1) programs. We are also grateful to the TSB for funding the CONVERT program.

References

1 K. Kohmoto, in *Phosphor Handbook*, ed. W. Yen, S. Shionoya and H. Yamamoto, CRC Press, Boca Raton, 2nd edn, 2007, p. 437.
2 T. Justel, H. Nikol and C. Ronda, *Angew. Chem., Int. Ed.*, 1998, **37**, 3085.
3 J. Silver, Metal Compounds as Phosphors, in *Comprehensive Coordination Chemistry II: The Synthesis, Reactions Properties and Applications of Coordination Compounds*, ed. J. A. McCleverty, Pergamon Press, New York, 2003, ch. 9.15, vol. 9, p. 689.
4 P. Zhang, A. Navrotsky, B. Gao, I. Kennedy, A. N. Clark, C. Lesher and Q. Liu, *J. Phys. Chem. C*, 2008, **112**, 932.
5 H. R. Hoekstra and K. A. Gingerich, *Science*, 1964, **146**, 1163.

6 A. Camenzind, R. Strobel and S. E. Pratsinis, *Chem. Phys. Lett.*, 2005, **415**, 193.
7 X. Qin, Y. Ju, S. Bernhard and N. Yao, *J. Mater. Res.*, 2005, **20**, 2960.
8 Y. C. Kang, D. J. Seo, S. B. Park and H. D. Park, *Jpn. J. Appl. Phys.*, 2001, **40**, 4083.
9 H. Chang, I. W. Lenggoro, K. Okuyama and T. O. Kim, *Jpn. J. Appl. Phys.*, 2004, **43**, 3535.
10 M. Okumura, M. Tamatani, A. K. Albessard and N. Matsuda, *Jpn. J. Appl. Phys.*, 1997, **36**, 6411.
11 W. Kraus and R. Birringer, *Nanostruct. Mater.*, 1997, **9**, 109.
12 D. K. Williams, B. Bihari, B. M. Tissue and J. M. McHale, *J. Phys. Chem. B*, 1998, **102**, 916.
13 L. Wang, Y. Pan, Y. Ding, W. Yang, W. L. Mao, S. V. Sinogeikin, Y. Meng, G. Shen and H. K. Mao, *Appl. Phys. Lett.*, 2009, **94**, 061921.
14 J. Zhang, H. Cui, P. Zhu, C. Ma, X. Wu, H. Zhu, Y. Ma and Q. Cui, *J. Appl. Phys.*, 2014, **115**, 023502.
15 V. Gourlaouen, G. Schnedecker, A. M. Lejus, M. Boncoeur and R. Collongues, *Mater. Res. Bull.*, 1993, **28**, 415.
16 G. Kaptay, *J. Nanosci. Nanotechnol.*, 2011, **12**, 1.
17 D. R. Johnson, *US Pat.*, US2014/0370293 A1, 2014.
18 D. den Engelsen, P. G. Harris, T. G. Ireland and J. Silver, *ECS J. Solid State Sci. Technol.*, 2014, **3**, R53.
19 X. Jing, T. Ireland, C. Gibbons, D. J. Barber, J. Silver, A. Vecht, G. Fern, P. Trogwa and D. C. Morton, *J. Electrochem. Soc.*, 1999, **146**, 4654.
20 D. den Engelsen, P. G. Harris, T. G. Ireland, R. Withnall and J. Silver, *ECS J. Solid State Sci. Technol.*, 2013, **2**, R201.
21 D. den Engelsen, G. R. Fern, T. G. Ireland, P. G. Harris, P. R. Hobson, A. Lipman, R. Dhillon, P. Marsh and J. Silver, *J. Mater. Chem. C*, 2016, **4**, 7026.
22 J. Wen, L. Hu, M. Yin and S. Xia, *Curr. Appl. Phys.*, 2012, **12**, 732.
23 J. B. Gruber, R. P. Leavitt, C. A. Morrison and N. C. Chang, *J. Chem. Phys.*, 1985, **82**, 5373.
24 J. Silver, M. I. Martinez-Rubio, T. G. Ireland, G. R. Fern and R. Withnall, *J. Phys. Chem. B*, 2001, **105**, 9107.
25 N. C. Chang, J. B. Gruber, R. P. Leavitt and C. A. Morrison, *J. Chem. Phys.*, 1982, **76**, 3877.
26 F. Vetrone, J.-C. Boyer, J. A. Capobianco, A. Speghini and M. Bettinelli, *Nanotechnology*, 2004, **15**, 75.
27 R. Withnall, J. Silver and T. G. Ireland, Proceedings of the XXIst International Conference on Raman Spectroscopy, 650 (2008).
28 J. Gouteron, D. Michel, A. M. Lejus and J. Zarembowitch, *J. Solid State Chem.*, 1981, **38**, 288.

